Monthly Notices
of the
ROYAL ASTRONOMICAL SOCIETY

Mon. Not. R. Astron. Soc. **402,** 335–344 (2010) doi:10.1111/j.1365-2966.2009.15873.x

Stellar population and dust extinction in an ultraluminous infrared galaxy at $z = 1.135$

K. Kawara,[1⋆] S. Oyabu,[2] Y. Matsuoka,[3] Y. Yoshii,[1] T. Minezaki,[1] H. Sameshima,[1] N. Asami,[1] N. Ienaka[1] and T. Kozasa[4]

[1]*Institute of Astronomy, the University of Tokyo, Osawa 2-21-1, Mitaka, Tokyo 181-0015, Japan*
[2]*Institute of Space and Astronautical Science, Japan Aerospace Exploration Agency, 3-1-1 Yoshinodai, Sagamihara, Kanagawa 229-8510, Japan*
[3]*Graduate School of Science, Nagoya University, Furo-cho, Chikusa-ku, Nagoya 464-8602, Japan*
[4]*Department of Cosmosciences, Hokkaido University, Sapporo 060-0810, Japan*

Accepted 2009 October 14. Received 2009 October 13; in original form 2009 June 29

ABSTRACT

We present the detailed optical to far-infrared (far-IR) observations of SST J1604+4304, an ultraluminous IR galaxy at $z = 1.135$. Analysing the stellar absorption lines, namely, the Ca II H & K and Balmer H lines in the optical spectrum, we derive the upper limits of an age for the stellar population. Given this constraint, the minimum χ^2 method is used to fit the stellar population models to the observed spectral energy distribution from 0.44 to 5.8 μm. We find the following properties. The stellar population has an age 40–200 Myr with a metallicity 2.5 $Z_\odot$. The starlight is reddened by $E(B - V) = 0.8$. The reddening is caused by the foreground dust screen, indicating that dust is depleted in the starburst site and the starburst site is surrounded by a dust shell. The IR (8–1000 μm) luminosity is $L_{\rm ir} = 1.78 \pm 0.63 \times 10^{12}\,{\rm L}_\odot$. This is two times greater than that expected from the observed starlight, suggesting either that 1/2 of the starburst site is completely obscured at UV-optical wavelengths, or that 1/2 of $L_{\rm ir}$ comes from active galactic nucleus (AGN) emission. The inferred dust mass is $2.0 \pm 1.0 \times 10^8\,{\rm M}_\odot$. This is sufficient to form a shell surrounding the galaxy with an optical depth $E(B - V) = 0.8$. From our best stellar population model – an instantaneous starburst with an age 40 Myr – we infer the rate of 19 supernovae per year. Simply analytical models imply that 2.5 $Z_\odot$ in stars was reached when the gas mass reduced to 30 per cent of the galaxy mass. The gas metallcity is 4.8 $Z_\odot$ at this point. The gas-to-dust mass ratio is then 120 ± 73. The inferred dust production rate is $0.24 \pm 0.12\,{\rm M}_\odot$ per SN. If 1/2 of $L_{\rm ir}$ comes from AGN emission, the rate is $0.48 \pm 0.24\,{\rm M}_\odot$ per SN. We discuss the evolutionary link of SST J1604+4304 to other galaxy populations in terms of the stellar masses and the galactic winds, including optically selected low-luminosity Lyman α-emitters and submillimeter selected high-luminosity galaxies.

Key words: dust, extinction – galaxies: evolution – galaxies: high-redshift – galaxies: individual: SST J1604+4304 – galaxies: starburst – galaxies: stellar content – cosmology: observations – infrared: galaxies.

1 INTRODUCTION

Infrared Astronomical Satellite (*IRAS*) observations discovered numerous IR galaxies. At bolometric luminosities $>10^{11}\,{\rm L}_\odot$, IR galaxies are the dominant population in the local Universe, being more numerous than optically selected starbursts, active galactic nuclei (AGNs) and quasars (Sanders & Mirabel 1996). By luminosity, IR galaxies are classified into luminous IR galaxies (LIRGs) with $L_{\rm ir} > 10^{11}\,{\rm L}_\odot$, ultraluminous IR galaxies (ULIRGs) with $L_{\rm ir} > 10^{12}\,{\rm L}_\odot$ and hyperluminous IR galaxies (HyLIRGs) with $L_{\rm ir} > 10^{13}\,{\rm L}_\odot$. The ratio of IR to visible luminosity, $L_{\rm ir}/L_{\rm B}$, increases with $L_{\rm ir}$ (Soifer et al. 1989). Although there is evidence that an optically buried AGN may exist in LIRGs, there is similarly strong evidence that enhanced star formation is ongoing (Armus et al. 1995; Sanders & Mirabel 1996). Heckman, Armus & Miley (1990) found that their optical spectroscopic data support the superwind model in which the kinetic energy provided by supernovae (SNe)

⋆E-mail: kkawara@ioa.s.u-tokyo.ac.jp

and winds from massive stars in starburst site drives a large-scale outflow.

The *Infrared Space Observatory* (*ISO*) source counts in the mid- and far-IR extended our knowledge of IR galaxies up to $z \sim 1$ (Oliver et al. 1997; Taniguchi et al. 1997; Kawara et al. 1998; Elbaz et al. 1999; Puget et al. 1999; Serjeant et al. 2000; Sato et al. 2003; Kawara et al. 2004), and revealed the number of ULIRGs rapidly grew with increasing redshift (Genzel & Cesarsky 2000; Chary & Elbaz 2001; Héraudeau et al. 2004; Oyabu et al. 2005).

The next large advance was made by the *Spitzer Space Telescope* with the sensitivity to probe IR galaxies at $z = 2$–4 (see review in Soifer, Helou & Werner 2008, and reference therein). Reddy et al. (2006), using deep *Spitzer* 24 μm observations, examined star formation and extinction in optically selected galaxies, near-IR-selected galaxies and submillimeter-selected galaxies (SMGs) at $z \sim 2$. *Spitzer* provided a powerful probe to measure redshifts of SMGs, the most luminous IR galaxy population as HyLIRGs (Pope et al. 2008a). Based on *Spitzer* mid-IR data, the diagnostic diagram to separate starburst- and AGN-dominated IR galaxies has been developed (e.g. Stern et al. 2005; Polletta et al. 2008; Pope et al. 2008b), and it is suggested that $L_{\rm ir}$ in SMGs as well as ULIRGs at $z \sim 2$ is dominated by star formation (Pope et al. 2008a), while many SMGs contain an AGN as evidenced by their X-ray properties. Dey et al. (2008) uncovered a new population of dust-obscured galaxies (DOGs). These galaxies have $L_{\rm ir}$ comparable to ULIRGs. However, their $L_{\rm ir}/L_{\rm B}$ is greater than local ULIRGs. DOGs and SMGs as well as high-redshift ($z \sim 1$) ULIRGs are generally considered to be young and massive galaxies, although the nature of the stellar populations is far from being understood. To understand the evolutionary link of these IR galaxies to optically selected and near-IR-selected galaxies, it is crucial to observe stellar absorption lines which indicate the age of the stellar populations.

During the course of searching for distant objects in a cluster field, SST J1604+4304 drew our attention with its red optical 3.6 μm colour. Follow-up study revealed this object is an ULIRG at $z \sim 1.135$ and its energy source is young stars with an age $<$200 Myr.

We present the data consisting of optical spectroscopy and photometry from the optical to far-IR in Section 2. We derive an age and metallicity of the stellar population, and show a foreground dust screen is plausible in Section 3. In Section 4, mid- and far-IR emission by dust and energetics are discussed. In Section 5, we discuss the inferred size of a dust shell surrounding the galaxy, the SN rate and metallicity expected from the broad-band spectral energy distribution (SED) analysis, and the dust production rate per SN. The evolutionary link of IR galaxies to optically selected galaxies is discussed based on the galactic wind models of elliptical galaxies.

We adopt $H_0 = 70\,{\rm km\,s^{-1}\,Mpc^{-1}}$, $\Omega_m = 0.3$ and $\Omega_\Lambda = 1 - \Omega_m$ throughout this paper. In this cosmology, the luminosity distance to the object is 7520 Mpc. The flux density F_ν is used in units of μJy, which is converted to AB magnitudes through the relation $m({\rm AB}) = -2.5\log({\rm F}_\nu) + 23.9$.

2 OBSERVATIONS AND DATA ANALYSIS

This work is based on the archival data taken by the *Spitzer Space Telescope*, the *Hubble Space Telescope* (*HST*) and the *Subaru* Telescope, and new photometric observations performed on the *United Kingdom Infrared Telescope* (*UKIRT*) and the *Multicolor Active Galactic Nuclei Monitoring* (*MAGNUM*)[1] telescope. In addition, the *Gemini Telescope North* was used to do optical spectroscopy.

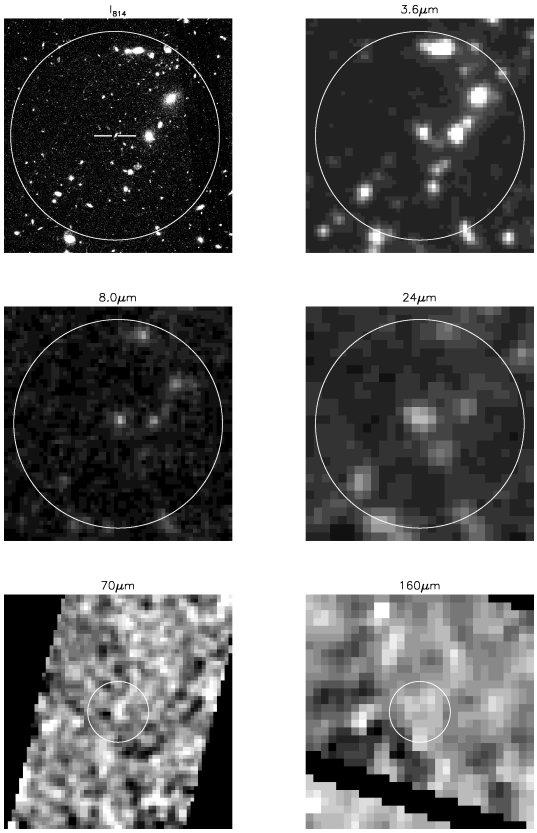

Figure 1. Images centred at SST J1604+4304, where the size is 70 × 70 arcsec^2 for I_{814}, 3.6, 8.0 and 24 μm, and 240 × 240 arcsec^2 for 70 and 160 μm. For all plots, north is at the top and east is to the left. We present 32 arcsec radius circles which are the size of the aperture used for MIPS 160 μm photometry. Two bars in the I_{814} image are used to indicate SST J1604+4304.

2.1 Target

SST J1604+4304 has been found at

RA $16^{\rm h}04^{\rm m}25\overset{\rm s}{.}538$, Dec. $+43^\circ04'26\overset{''}{.}55$,

in the J2000 system in a field observed with the *Spitzer* Infrared Array Camera (IRAC) instrument. The optical counterpart in the *HST* data is located within the 0.4 arcsec offset accuracy requirements of *Spitzer* (Werner et al. 2004). Images of SST J1604+4304 are given in Figs 1 and 2. The broad-band fluxes are given in Table 1. SST J1604+4304 is only 32 arcsec away from the centre of the massive galaxy cluster CL 1604+4304 at $z = 0.90$ (Gal & Lubin 2004). Based on a weak-lensing analysis, Margoniner et al. (2005) find the mass contained within projected radius R is (3.69 ± 1.47)$[R/(500\,{\rm kpc})]$ × $10^{14}\,{\rm M}_\odot$, corresponding to an inferred velocity dispersion 1004 ± 199 km s^{-1}. Thus, using a singular isothermal sphere, we obtain the magnification $m = 1.17 \pm 0.09$ for SST J1604+4304 (Schneider, Ehlers & Falco 1992).

[1] This telescope is dedicated to the *Multicolor Active Galactic Nuclei Monitoring* (*MAGNUM*) project and is installed at the Haleakala Observatories in Hawaii (Yoshii 2002).

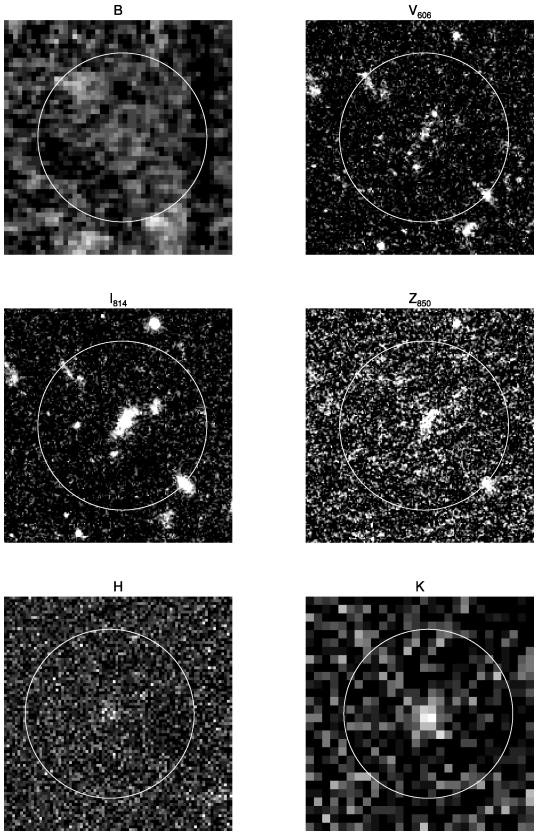

Figure 2. 10×10 arcsec^2 images centred at SST J1604+4304. For all plots, north is at the top and east is to the left. We present 3.7 arcsec radius circles which are the size of the aperture used for IRAC 3.6–8.0 μm photometry.

Table 1. Multiwavelength photometry of SST J1604+4304.

Filter[a] band	Total flux (μJy)	$R^b_{\rm ph}$ (arcsec)	Instrument	UT (yy/mm)
V_{606}	0.224 ± 0.062	1.2	*HST* ACS	03/08
I_{814}	1.05 ± 0.08	1.2	*HST* ACS	03/08
Z_{850}	1.53 ± 0.13	1.2	*HST* ACS	07/02
3.6 μm	60.35 ± 3.16	3.7	*Spitzer* IRAC	04/03
4.5 μm	53.76 ± 2.79	3.7	*Spitzer* IRAC	04/03
5.8 μm	55.11 ± 4.07	3.7	*Spitzer* IRAC	04/03
8.0 μm	65.68 ± 5.36	3.7	*Spitzer* IRAC	04/03
24 μm	319 ± 18.4	7.0	*Spitzer* MIPS	04/03
70 μm	2150 ± 870	16	*Spitzer* MIPS	04/03
160 μm	$32\,000 \pm 14\,000$	32	*Spitzer* MIPS	04/03
B	0.0803 ± 0.013	1.2	*Subaru* SUP	00/06
V	0.111 ± 0.015	1.2	*Subaru* SUP	05/05
R_c	0.218 ± 0.018	1.2	*Subaru* SUP	01/04,05
I_c	0.689 ± 0.042	1.2	*Subaru* SUP	01/04
z	2.29 ± 0.21	1.2	*Subaru* SUP	01/06
H	5.40 ± 1.19	1.2	*UKIRT* UIST	06/02
K	20.06 ± 3.35	1.2	*MAGNUM* MIP	06/08
20 cm	<0.66 mJy[c]	2.7	*VLA*[e]	1995
0.2–2 keV	<2.1[d]	15	*XMM*[f]	02/02
2–10 keV	<15[d]	15	*XMM*[f]	02/02

[a] V_{606}, I_{814}, and Z_{850} denote F606W, F814W and F850LP, respectively.
[b] The radius of the photometric apertures which were used to obtain the total fluxes.
[c] To 3σ.
[d] To 3σ in units of 10^{-15} erg cm^{-2} s^{-1}.
[e] From the FIRST survey (White et al. 1997).
[f] Observed by Lubin, Mulchaey & Postman (2004). The Flux Limits from Images from XMM-Newton (FLIX) online server was used to derive the upper limit.

2.2 *Spitzer* data

All IRAC and Multiband Imaging Photometer for Spitzer (MIPS) data sets were retrieved from the *Spitzer* public archive. The IRAC data consist of four broad-band images at 3.6, 4.5, 5.8 and 8.0 μm. The field of view is nearly 5.2×5.2 arcmin^2 with a linear scale of approximately 1.22 arcsec pixel^{-1}. The reader is referred to Fazio et al. (2004) for a complete report on the in-flight performance of IRAC. In the pipeline processing, 10 Basic Calibrated Data (BCD) Flexible Image Transport System (FITS) images were co-added into a single mosaic image per band with a technique similar to 'drizzle'. The total effective exposure time is 1936 s pixel^{-1} per band. Photometry was performed using a 3 pixel (3.7 arcsec) radius aperture. As can be seen in the 3.6 μm image in Fig. 1, there are two sources which can contribute to the flux within the photometric aperture; a faint source is at 6.5 arcsec to the south-west and a bright source 10 arcsec to the west. Using the point-spread function, which is available on the IRAC website, their contributions were estimated to be 3.1–4.3 per cent of the flux of SST J1604+4304 depending on the photometric band. The total fluxes after applying the aperture correction are given in Table 1. The quoted errors include 5 per cent absolute calibration uncertainty that SSC[2] recommends for general observers. Note that the colour correction is very small and ignored.

The MIPS data were taken at 24, 70 and 160 μm in 2004 March. In the pipeline processing, the mapped BCD data were rebinned and co-added to a single image with a linear pixel scale of 2.5, 4.0 and 4.0 arcsec pixel^{-1} for 24, 70 and 140 μm, respectively. The total integration times are 93, 53 and 84 s pixel^{-1}. In the following analysis, we use the following post-BCD products, namely, mosaic images for 24 μm and filtered mosaic images for 70 and 160 μm. 24 μm photometry was performed using a 7 arcsec radius aperture. The contributions, to the flux within the photometric aperture, from the two sources (see the 24 μm image in Fig. 1), located approximately at 15 arcsec to the west-northwest and 13 arcsec to the south-west, were estimated using the point-spread function on the MIPS website. Their contributions are 9 per cent of the flux within the aperture. Then, the colour correction for 500K blackbody and the aperture correction were applied.

MIPS 70 and 160 μm photometry was performed using 16 and 32 arcsec radius apertures, respectively. As seen in Fig. 1, SST J1604+4304 is faint in the far-IR. We measured sky fluxes with the same aperture at 10 or 11 positions along the annulus with radii of 36–72 arcsec at 70 μm and 96–150 arcsec at 160 μm. The flux averaged over these sky fluxes was subtracted from the flux measured within the object aperture centred at SST J1604+4304. The aperture correction and the colour correction for 30K were applied. The detections are 2.5σ and 5.0σ at 70 and 160 μm, respectively. As seen in the 24 μm image in Fig. 1, there are several 24 μm sources within the 160 μm photometry aperture. Judging from their [3.6 μm]–[24 μm] colour and 70 and 160 μm brightness at their respective positions, the source at 13.5 arcsec to the west-northwest, the only source as red as SST J1604+4304, may contribute 1/3 of the flux within the aperture at most. The 160 μm flux is 38.4 ± 7.65 mJy if the contributions from this source can be ignored, while the flux is 25.6 ± 7.65 mJy if this source contributes 1/3 of the

[2] See Infrared Array Camera Data Handbook.

flux within the aperture. The real flux of SST J1604+4304 should be between them, and thus the flux is 32 ± 14 mJy. The aperture correction and the colour correction for 30K blackbody were applied. Note that the 24 μm error in Table 1 includes 4 per cent absolute calibration uncertainty.[3]

2.3 Optical imaging data

The V_{606}, I_{814} and Z_{850} image data were retrieved from the *HST* public archive, where V_{606}, I_{814} and Z_{850} denote the $F606W$, $F814W$ and $F850LP$, respectively. The Advanced Camera for Surveys (ACS) Wide Field Camera (WFC) was used, which covers a field of 3.4 × 3.4 arcmin^2 with a scale of 0.05 arcsec pixel^{-1}. Four image data were combined into a single co-added image per band. The total exposure times are 4840 s pixel^{-1} for V_{606} and I_{814} and 6000 s pixel^{-1} for Z_{850}. The I_{814} image in Fig. 2 shows that SST J1604+4304 has irregular morphology extending 1.6 arcsec in the north-west direction with a 0.6 width. To determine the total flux of this object, I_{814} photometry was performed using 0.8, 1.0, 1.2 and 2.0 arcsec radius apertures. The I_{814} flux grows from 0.8 to 1.2 arcsec, while it barely increase from 1.2 to 2.0 arcsec. Note that contributions from the two nearest sources were subtracted from the flux measured with the 2.0 arcsec radius aperture. Thus, the flux measured with the 1.2 arcsec radius aperture represents the total flux of SST J1604+4304. The ratio of the flux with a 0.8 arcsec aperture to a 1.2 arcsec aperture is 1.24 ± 0.05. V_{606} and Z_{850} photometry was performed using a 0.8 arcsec aperture. The resultant fluxes were converted to the total fluxes by multiplying 1.24 ± 0.05, because we did not measure significant changes in optical colours across the target. The total fluxes are given in Table 1. The errors in Table 1 include the error of aperture conversion from 0.8–1.2 arcsec and the correction for correlated noise in drizzling.

Subaru B, V, R_c, I_c, z data were retrieved from the Subaru-Mitaka-Okayama-Kiso Archive (SMOKA). The data were taken with Suprime-Cam (SUP) imager which has a field of view of 34 × 27 arcmin^2 with a scale of 0.2 arcsec pixel^{-1}. The total exposure time is 2880, 2520, 3600, 1680, 3300 s pixel^{-1} after co-adding 4 to 11 image frames, using the standard SUP script (Yagi et al. 2002). Flux scaling was performed observing 11 standard stars given by Majewski et al. (1994). I_c photometry were performed using three apertures with a radius of 1.0, 1.2 and 2.0 arcsec, and it was confirmed the *Subaru* I_c brightness distribution is identical to that measured at the *HST* I_{814} photometry band. Thus, we use the 1.2 arcsec radius aperture centred on SST J1604+4304 to obtain the fluxes given in Table 1. The errors in Table 1 include 5 per cent photometric uncertainty.

2.4 H/K imaging observations

The H-band image was taken with the UKIRT 1–5 μm Imager Spectrometer (UIST) in 2006 February. UIST was used in the imaging mode with a field of view of 2 × 2 arcmin^2 and a scale of 0.12 arcsec pixel^{-1}. The total exposure time is 1800 s pixel^{-1} after co-adding individual image data with an integration time of 60 s. The sky condition was photometric with 0.6 arcsec seeing. The K-band image was taken with the multicolour imaging photometer (MIP) on the 2 m *MAGNUM* telescope (Kobayashi et al. 1998; Minezaki et al. 2004) in 2006 August. MIP has a field of view of 1.5 × 1.5^2 with a linear scale of 0.346 arcsec pixel^{-1}. The total integration time is 2340 s pixel^{-1} after co-adding individual image data. The weather condition was photometric with 1 arcsec seeing. Flux calibration was performed using 2MASS 16042631+4303413 (H = 14.36, K = 14.39) observed simultaneously with SST J1604+4304. Photometric uncertainty is 5 and 9 per cent for H and K, respectively.

[3] Multiband Imaging Photometer for Spitzer (MIPS) Data Handbook.

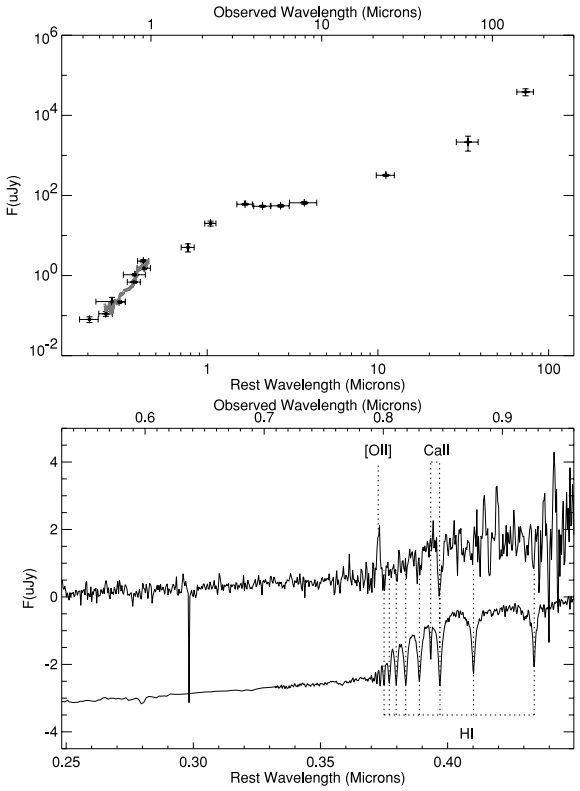

Figure 3. The top panel shows UV to far-IR SED for SST J1604+4304. The broad-band data are shown along with the median-smoothed optical spectrum (grey) taken with Gemini-North GMOS. The bottom panel shows the optical spectrum (top) together with the synthetic spectrum (bottom) at an age of 400 Myr, reddened by $E(B-V) = 0.6$.

2.5 Optical spectroscopy

Optical spectroscopy was carried out using the Gemini Multi-Object Spectrograph (GMOS) on the Gemini-North telescope in 2007 August. The R150_G5306 grating was used along with the OG151_G036 filter, covering 5000–10 000 Å simultaneously with 6.96 Å pixel^{-1} after binned by 4 in the dispersion direction. The different wavelength centres (8200 and 8250 Å) were set to fill the CCD gaps. A 1.0 arcsec width slit was set so that the dispersion direction is perpendicular to the long axis of the target. Seven 1800 s exposures were taken in the Nod & Shuffle mode. Data were reduced in a standard manner using the IRAF GEMINI.GMOS package. The sky subtraction was made with the GNSSKYSUB routine. Wavelengths were scaled with CuAr spectra and the relative photometric calibration was performed using the standard star (HZ44). The results are shown in the bottom panel of Fig. 3. The spectrum which is median-smoothed with a width of 40 pixles (i.e. ∼280 Å) is compared with the photometry from the images in the top panel of Fig. 3. The two measurements agree with each other.

3 STELLAR POPULATIONS AND DUST EXTINCTION

3.1 Spectroscopic diagnosis

The redshift of SST J1604+4304 is 1.135, as identified in Fig. 3. The synthetic spectrum is also shown for comparison. This spectrum was made using the instantaneous-burst model (Bruzual & Charlot 2003) at an age 400 Myr, reddened by $E(B-V) = 0.6$. The UV-optical spectrum is characterized by stellar absorption lines, which are H_ϵ at 3970 Å, H_ζ at 3889 Å, and probably higher order lines in the H I Balmer series as well as possible presence of the Ca II HK absorption lines at 3968 and 3934 Å. The emission line of [O II] at 3727 Å is detected. No lines indicating the presence of an AGN, such as Mg IIλ2798 and [Ne V]λ3346, 3426, are detected. The 3σ upperlimit of the Mg II equivalent width (EW) is 22 Å, assuming a full width at half-maximum 6000 km s^{-1} for the line width. This upper limit is small compared to 52 Å which is the Mg II EW of the composite spectrum obtained from 184 quasi-stellar objects (QSOs) by Telfer et al. (2002). There are no signs indicating AGN emission at other wavelengths including X-ray and radio as shown Table 1. Thus, we assume that the UV-optical spectrum is dominated by starlight.

The amplitude of the 4000 Å discontinuity is known as a useful tool to measure the age of stellar populations (e.g. Bruzual 1983; Matsuoka et al. 2008). However, it is not simple to correct for the reddening for heavily obscured objects like SST J1604+4304. Alternatively, the EWs of Ca II K and Balmer H lines are used to scale ages of star clusters (Rabin 1982; Santos & Piatti 2009). Here, we use the index which is defined as D(Ca II) = 2 × EW(Ca II K)/[EW(H_ζ)+EW(Ca II H + H_ϵ)], where EW(Ca II K) is the EW for the Ca II K line, EW(H_ζ) for the H_ζ line and EW(Ca II H + H_ϵ) for the blends of the Ca II H and H_ϵ lines. The EW is obtained by integrating across the line as EW $= \int_{\lambda 1}^{\lambda 2}(F_\lambda^c - F_\lambda)\mathrm{d}\lambda/\overline{F^c}$, where $\overline{F^c} = \int_{\lambda 1}^{\lambda 2} F_\lambda^c \mathrm{d}\lambda/(\lambda 2 - \lambda 1)$. ($\lambda$ 1, λ2) in Å is (3871, 3909), (3926, 3940) and (3951, 3990) for H_ζ, Ca II K and Ca II H + H_ϵ, respectively. F_λ is the observed flux density and $F^c{}_\lambda$ is the continuum across the line, which is derived by fitting a linear function to assumed continuum points on either side of the line profile. Thus, we have D(Ca II) = 0.03 ± 0.11 for SST J1604+4304, where EW(Ca II K) = 0.4 ± 1.4 Å, EW(H_ζ) = 7.6 ± 2.1 Å and EW(Ca II H + H_ϵ) = 16.7 ± 2.2 Å.

Fig. 4 shows D(Ca II) measured in synthetic spectra for various metallicities as a function of ages of stellar populations. The synthetic spectra were obtained based on the instantaneous-burst models (Bruzual & Charlot 2003) for metallicities $Z = 0.005$, 0.02, 0.2, 0.4, 1 and 2.5 $Z_\odot$. The horizontal line shows the constraint from the observed D(Ca II) at 1, 2 and 3σ upper limits. This diagram indicates that the inferred age of SST J1604+4304 depends on the metallicity; the 3σ constraint is <1000 Myr for $Z = 0.2\,Z_\odot$, <750 Myr for 0.4 $Z_\odot$, <600 Myr for 1.0 $Z_\odot$ and <400 Myr for 2.5 $Z_\odot$.

The [O II]λ3727 line flux is 5.5 ± 0.8 × 10^{-17} ergs cm^{-2} s^{-1}. Its implications for the star formation rate (SFR) will be discussed later.

3.2 Analysis of the UV to near-IR SED

We explore the nature of stellar populations and interstellar material in SST J1604+4304, by fitting model spectra of stellar population models to the observed SED from the *B* to 5.8 μm band. The 8.0 μm band is not included in this analysis, because emission from hot dust would be significant in this band. The evolutionary synthesis codes (Bruzual & Charlot 2003) are used to generate synthetic spectra of evolutionary stellar population models. The initial mass function (IMF) by Chabrier (2003) (his table 1) is adopted with a lower and upper mass cut-off at 0.1 and 100 $M_\odot$, respectively.

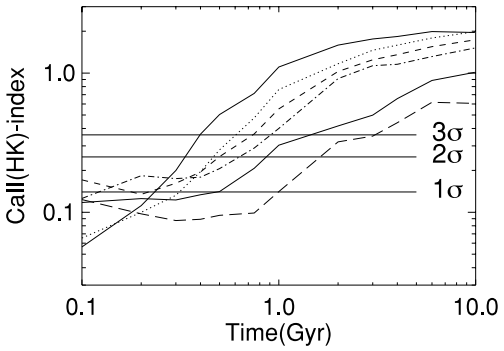

Figure 4. The D(Ca II) index as a function of ages of stellar populations. The index is defined as D(Ca II) = 2 × EW(Ca II K)/EW(H_ζ+Ca II H + H_ϵ). The metallicities are 0.005 $Z_\odot$ (long dashes), 0.02 $Z_\odot$ (dash–dot–dot–dot), 0.2 $Z_\odot$ (dash–dot), 0.4 $Z_\odot$ (dashed), 1.0 $Z_\odot$ (dotted) and 2.5 $Z_\odot$ (solid). The three horizontal bar indicate the observed upper boundary of the D(Ca II) index at 1, 2 and 3σ upper limits.

We use two extinction laws, namely, the starburst extinction curve by Calzetti (2001) and the Milky Way (MW) extinction curve by Draine (2003). The starburst extinction curve was derived from the data in the UV and optical wavelength range of local starbursts and blue compact galaxies (Calzetti, Kinney & Storchi-Bergmann 1994). We consider two extreme cases of geometrical distribution of dust, namely, a *foreground dust screen* and *internal dust model*. In case of the foreground dust screen, dust is uniformly distributed in the screen which is physically distant from star clusters, so we observe $I^0 e^{-\tau}$ where τ is the optical depth of the dust screen and I^0 is unextincted radiation. In the internal dust model, dust and stars are uniformly mixed and the model schematizes the situation in which dust is purely internal to the staburst site, so we observe $I^0(1 - e^{-\tau(1-\gamma)})/[\tau(1-\gamma)]$, where γ is the albedo. Note that we assume the isotropic scattering.

Calzetti (2001) gives the extinction curve in a narrow range from 0.12–2.2 μm. To analyse multiwavelemgth data from the UV to IR, the extinction curve should be extended to wavelengths >2.2 μm. The analytical expression given by Calzetti (2001) cannot be used for this extension, because the expression makes extinction values sharply drop beyond 2.2 μm. The Calzetti's extinction curve is almost identical to the Draine (2003) MW curve from 0.6–1.6 μm. We thus extend the Calzetti's curve to longer wavelenths by adopting the MW extinction curve for wavelengths ≥1.6 μm. In addition, because Calzetti (2001) does not provide the albedo, we adopt the albedo given in Draine (2003) for the Calzetti's extinction law with removing the dip in the albedo which is attributed to the familiar 2175 Å feature.

We start with instantaneous-burst models where all stars formed at once. The best model fit was searched for the observed SED by simultaneously optimizing the parameters, i.e. flux scales, ages of stellar populations *t*, extinction $E(B-V)$ intrinsic to SST J1604+4304 and metallicities of the stellar populations (*Z*). The ranges of the parameters are $t = 0.01$–6 Gyr, $E(B-V) = 0.0$–2.0 for the foreground dust screen and $E(B-V) = 0.0$–12.0 for the internal dust model, and $Z = 0.005$–2.5 $Z_\odot$. It is noted that 5 per cent of the flux was added in quadratic form to the photometric error

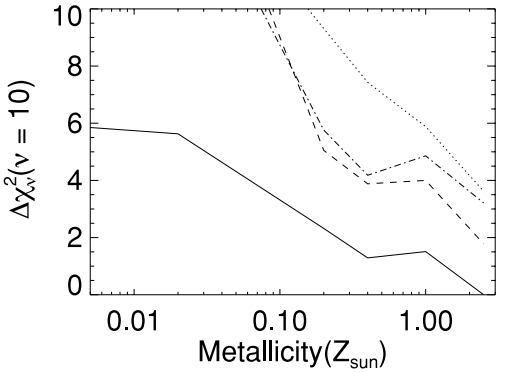

Figure 5. $\Delta\chi^2_\nu$ versus metallicity, where $\Delta\chi^2_\nu = \chi^2_\nu - \chi^2_\nu(\mathrm{min})$. $\chi^2_\nu(\mathrm{min})$, the smallest reduced χ^2 (=5.2), is obtained for $Z = 2.5\ Z_\odot$ with the foreground Calzetti's dust screen. The solid line shows $\Delta\chi^2_\nu$ for foreground dust screens with the Calzetti's extinction law, the dotted line for foreground dust screens with the MW extinction law, the dashed line for internal dust models with the Calzetti's extinction law and the dash dotted line for internal dust models with the MW extinction law. Note that χ^2_ν was minimized for a given metallicity by changing ages t and $E(B-V)$.

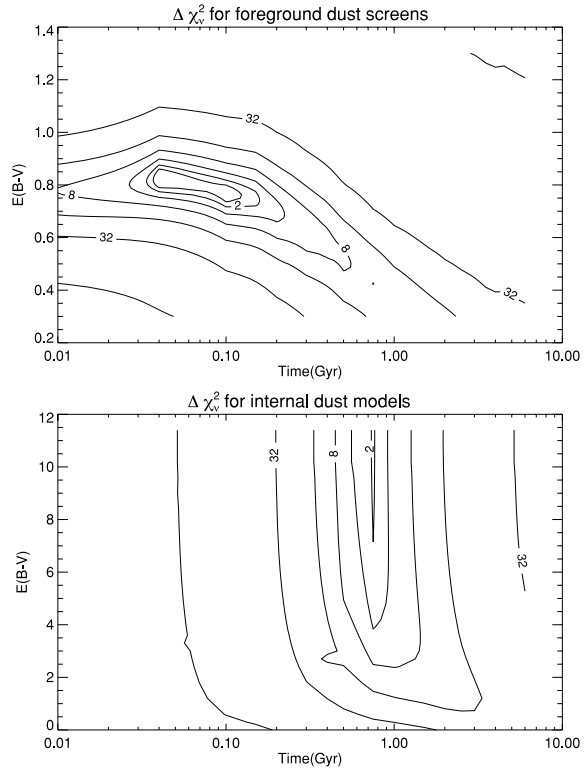

Figure 6. $\Delta\chi^2_\nu$ maps for foreground dust screens (top) with $2.5\,Z_\odot$ instantaneous-burst models and internal dust models (bottom). The Calzetti's extinction law was used. Note that internal dust models require much longer ages of stellar populations than those of uniform dust screens.

quoted in Table 1 to avoid too small and non-realistic photometric error.

The results are summarized in Figs 5 and 6. The best fit was obtained for $t = 40$ Myr, $E(B-V) = 0.8$ and $Z = 2.5\,Z_\odot$ with the foreground dust screen combined with the Calzetti (2001) extinction law, resulting in a reduced chi square χ^2_ν of 5.2. This χ^2_ν is the minimum among all the models analysed in this work. We

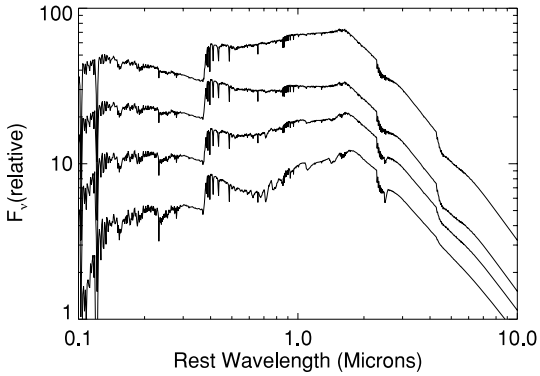

Figure 7. Instantaneous-burst models with an age 40 Myr for various metallicities. From the top to the bottom, the synthetic spectra for $Z = 0.2$, 0.4, 1.0 and $2.5\,Z_\odot$ are given.

thus refer to this minimum as $\chi^2_\nu(\mathrm{min}) = 5.2$, and the increment χ^2_ν relative to $\chi^2_\nu(\mathrm{min})$ is represented as $\Delta\chi^2_\nu = \chi^2_\nu - \chi^2_\nu(\mathrm{min})$ (Avni 1976). The approximate values of $\Delta\chi^2_\nu$ are 1.15, 1.83 and 2.77 for 68, 95 and 99.6 per cent confidence in this case (i.e. the degree of freedom is $\nu = 10$).

The foreground dust screen with the MW extinction law is ruled out, because of the too large $\Delta\chi^2_\nu$ (>3). The internal dust models are ruled out either for two reasons: (i) inferred ages of the stellar populations are too large to be fit within the range allowed by the D(Ca II) index; (ii) $\Delta\chi^2_\nu$ is too large, i.e. $\Delta\chi^2_\nu > 3$ for the $Z \leq Z_\odot$ models and $\Delta\chi^2_\nu = 1.8$ for $Z = 2.5\,Z_\odot$. For example, the best model for the internal dust geometry is obtained for $Z = 2.5\,Z_\odot$. As can be seen in the bottom panel of Fig. 6, the inferred age is $t = 0.7$–0.8 Gyr. This age is not allowed because the age range must be <400 Myr, corresponding to the 3σ D(Ca II) limit for $Z = 2.5\,Z_\odot$, as indicated in Fig. 4. Fig. 5 shows that models with a rich metallicity give better fit to the data than those with a low metallicity. The sensitivity to metallicity arises from the broad concave feature around rest 7000 Å, as shown in Fig. 7. This feature is very weak in low-metallicity spectra and becomes outstanding towards the high metallicity.

We also examined models with the exponentially declining SFR, which is represented by $\tau_e^{-1}\exp(-t/\tau_e)$, where τ_e is the e-folding time-scale and t is the time after the onset of the first star formation. τ_e ranges from 0.01–5.0 Gyr in a step of 0.5 dex and t from 0.01–7 Gyr. The Calzetti's extinction law was used in the uniform dust screen geometry. All models with $Z \leq Z_\odot$ are rejected because they have $\Delta\chi^2_\nu > 2$. The D(Ca II) index allows $2.5\,Z_\odot$ models to have $t \leq 500$ Myr, corresponding to 3σ D(Ca II) limit for exponentially declining star formation.[4] When τ is fixed and the other parameters are changed, the smallest values of χ^2_ν are obtained for $E(B-V) \simeq 0.8$. In addition, t correlates well with τ. Using this correlation, we found $\tau \leq 1000$ Myr. Applying another constraint $\Delta\chi^2_\nu < 1$, corresponding to the $1\,\sigma$ deviation, we find that $\tau = 90$ Myr and $t = 200$ Myr are allowed for the exponentially declining star formation models.

The results are summarized in Table 2. In Fig. 8, we plot the best fit (i.e. $\Delta\chi^2 = 0$) instantaneous-burst model with $Z = 2.5\,Z_\odot$ and an age of 40 Myr.

[4] For a given age of galaxies, D(Ca II) is smaller in exponentially declining star formation than in instantaneous-burst, because in exponentially declining star formation stars are continuously forming.

Table 2. Pure star formation with no AGN for SST J1604+4304.

Quantity	Instantaneous[a]	E-declining[b]
$E(B-V)^c$	0.83	0.79
$Z(Z_\odot)^d$	2.5	2.5
τ_e (Myr)^e	–	90
t (Myr)^f	40	200
$L/M^g{}_*$	28	14
L_{ir} ($L_\odot$)	$1.78 \pm 0.63 \times 10^{12}$	$1.78 \pm 0.63 \times 10^{12}$
M_* ($M_\odot$)	$6.4 \pm 2.3 \times 10^{10}$	$12.7 \pm 4.5 \times 10^{10}$
$\Delta\chi^2_\nu$	0.0	0.98

[a]Instantaneous-burst models where stars form all at once.
[b]Exponentially declining star formation models with SFR $\propto \tau_e^{-1} e^{-t/\tau_e}$, where t is the time after the onset of the initial star formation and τ_e is the e-folding time-scale.
[c]The Calzetti (2001) extinction law is used in a foreground dust screen.
[d]Metallicity of the stellar populations.
[e]e-folding time-scale for SFR.
[f]Time after the onset of the initial star formation.
[g]Luminosity to mass ratio in solar units, where M_* is a stellar mass at $t = 0$.

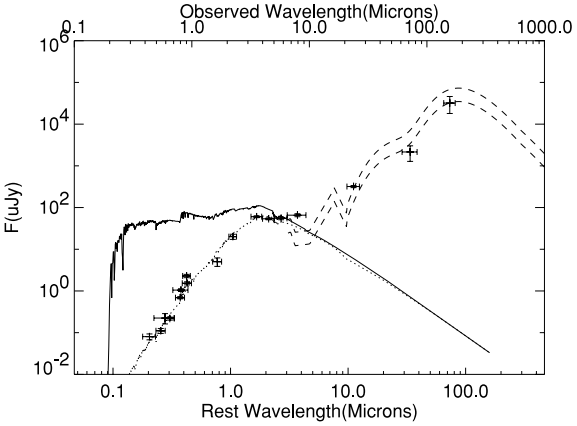

Figure 8. UV to far-IR SED for SST J1604+4304 along with the best-fitting stellar population model with the Arp 220 template. The solid line shows the unreddened stellar spectrum and the dotted line the stellar spectrum with the uniform dust screen $E(B-V) = 0.8$. This is the best-fitting instantaneous-burst model for an age 40 Myr. The dashed lines represent the Arp 220 template fitted to three data points at 24, 70 and 160 μm (upper) and two data points at 70 and 160 μm (lower) , where the template is made based on Carico et al. (1990), Rigopoulou et al. (1996) and Klaas et al. (1997).

4 DUST EMISSION AND ENERGETICS

4.1 Infrared luminosity

As shown in Fig. 8, dust emission is prominent at the 24, 70 and 160 μm bands. Because no data are available longwards of 160 μm, we fit the Arp 220 template to these data points to estimate the bolometric IR luminosity. The template is made based on Carico et al. (1990), Rigopoulou, Lawrence & Rowan-Robinson (1996) and Klaas et al. (1997). In Fig. 8, the upper dashed line represents the template which is fitted to the three data point at 24, 70 and 160 μm, while the lower dashed line shows the template fitted to the two data points at 70 and 160 μm. The former seems to overestimate the luminosity, while the latter could underestimate the luminosity. We adopt the average of these two values for the real luminosity. Then, the 8–1000 μm bolometric luminosity is $L_{ir} = 1.78 \pm 0.63 \times 10^{12}\,L_\odot$, classifying SST J1604+4304 as an ULIRG. Note that L_{ir} includes the correction for the flux magnification by cluster Cl 1604+4304, which is estimated to be 1.17.

4.2 Energetics

The stellar luminosity, which is inferred from the best instantaneous-burst model, is $8.9 \times 10^{11}\,L_\odot$, accounting for only 1/2 of L_{ir}. If star formation activity dominates the bolometric output, the significant part of the starburst site is hidden by very opaque dust extinction which we cannot observe at UV to near-IR wavelengths, implying the dust distribution in the foreground screen is clumpy. Otherwise, 1/2 of L_{ir} is fuelled by AGN emission.

The *XMM–Newton* X-ray 0.2–10 keV and VLA radio 20 cm data listed in Table 1 do not support the AGN emission in SST J1604+4304. However, it should be noted that the X-ray and radio observations are not deep enough to rule out a significant contribution from the AGN to the bolometric luminosity L_{ir}. Mid-IR data are widely used to search for obscured AGNs, because these wavelengths are much less affected by extinction and can penetrate through the dusty atmospheres surrounding the AGNs (Park et al. 2008). Using the $f_\nu(8\,\mu m)/f_\nu(4.5\,\mu m)$ versus $f_\nu(24\,\mu m)/f_\nu(8\,\mu m)$ AGN diagnostic, Ivison et al. (2004) and Pope et al. (2008a) showed that IR galaxies having $f_\nu(8\,\mu m)/f_\nu(4.5\,\mu m) < 1.9$ are starburst dominated in the mid-IR. SST J1604+4304 having $f_\nu(8\,\mu m)/f_\nu(4.5\,\mu m) = 1.22 \pm 0.12$ is thus starburst dominated. SST J1604+4304 has bluer mid-IR colours than those of obscured AGNs and type 1 QSOs studied by Polletta et al. (2008). Stern et al. (2005) showed a [3.6 μm]–[4.5 μm] versus [5.8 μm]–[8.0 μm] colour–colour diagram for identifying AGNs. SST J1604+4304 with [3.6 μm]– [4.5 μm](Vega) = 0.35 ± 0.08 and [5.8 μm]–[8.0 μm](Vega) = 0.85 ± 0.12 lies on the edge of the region which empirically separates AGNs from normal galaxies. Yan et al. (2007) performed mid-IR spectroscopy of IR luminous galaxies at $z \sim 2$ with the sample selection criteria $\nu f_\nu(24\,\mu m)/\nu f_\nu(8\,\mu m) \geq 3.16$. SST J1604+4304 having $\nu f_\nu(24\,\mu m)/\nu f_\nu(8\,\mu m) = 1.6$ does not meet the criteria of their sample. In conclusion, it is likely that mid- and far-IR emission is starburst-dominated in SST J1604+4304, however we are unable to rule out the presence of AGN emission.

We compare the UV to far-IR SED of SST J1604+4304 with those of three starburst-dominated galaxies, namely, M82 (local starburst), Arp220 (local ULIRG) and MIPS J142824.0+352619 ($z = 1.3$ HyLIRG) in Fig. 9. MIPS J142824.0+352619 with $L_{ir} = 3.2 \times 10^{13}\,L_\odot$ lacks any trace of AGN activity and has large polycyclic aromatic hydrocarbon (PAH) features and rich molecular gasses, indicating starburst-dominated mid-IR emission (Desai et al. 2007). As seen in Fig. 9, there is a striking similarity between SST J1604+4304 and MIPS J142824.0+352619 in the overall SEDs from the UV to far-IR.

4.3 Dust mass

The dust mass M_{dust} is related to the flux density f_ν as $M_{dust}/f_\nu = D^2/[\kappa_\nu B_\nu(T_{dust})]$ in the rest frame, where D is the distance to the source and κ_ν is the absorption cross-section per unit dust mass (e.g. Oyabu et al. 2009). When a modified blackbody spectrum $\nu^\beta B_\nu(T_{dust})$ is applied, β and T_{dust} should be used together as a set, because M_{dust} depends on $\kappa_\nu B_\nu(T_{dust})$, but not on $B_\nu(T_{dust})$ alone. To derive M_{dust}, we will use the dust model for the MW in the far-IR (Draine 2003) in which $\kappa_\nu \propto \nu^2$ or $\beta = 2$. Assuming $\beta = 2$, we obtain 32.5 K for the Arp 220 template and 35K

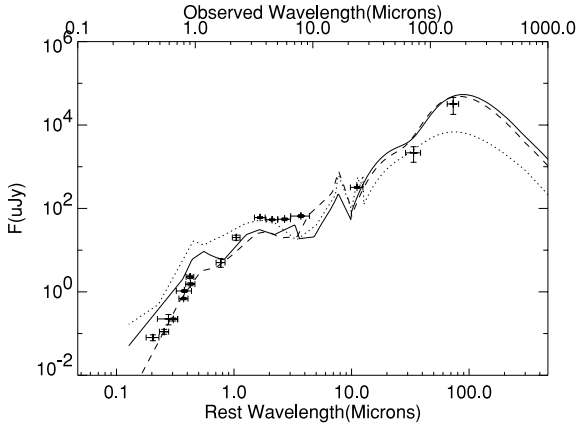

Figure 9. UV to far-IR SED for SST J1604+4304 compared with those of starburst-dominated galaxies, M 82 (dot local starburst), Arp 220 (solid local ULIRG), MIPS J142824.0+352619 (dash $z = 1.3$ HyLIRG). M82 data come from Willner et al. (1977), Dale et al. (2001), Hughes, Gear & Robson (1994), Leeuw & Robson (2009) and Weedman, Charmandaris & Zezas (2004), Arp 220 from Carico et al. (1990), Rigopoulou et al. (1996) and Klaas et al. (1997), and MIPS J142824.0+352619 from Desai et al. (2007) and Borys et al. (2006).

for MIPS J142824.0+352619. This range of temperatures implies $M_{\rm dust} = 2.0 \pm 1.0 \times 10^8\,{\rm M}_\odot$ for SST 1604+4304, where the uncertainty is dominated by the error in the 160 μm flux.

5 DISCUSSION

For simplicity, we temporarily assume that SST J1604+4304 is purely powered by star formation and at the end we will discuss the impact if SST J1604+4304 is AGN-dominated.

5.1 Stellar mass

The stellar mass M_* can be estimated as $L_{\rm ir}/(L/M_*)$, where L/M_* is the luminosity to mass ratio for the stellar population models. Thus, we have $M_* = 6 - 13 \times 10^{10}\,{\rm M}_\odot$ at $t = 0$ as listed in Table 2. If this stellar mass was constantly built up during 40–200 Myr, the SFR = 600–1650 $\,{\rm M}_\odot\,{\rm yr}^{-1}$. Using the calibrations of SFR in terms of the [O II] luminosity (Kennicutt 1998), after dereddening the [O II] flux, implies 13–500 $\,{\rm M}_\odot\,{\rm yr}^{-1}$. Considering that we are only looking at 1/2 of the starburst activity in the optical, we obtain SFR = 26–1000 $\,{\rm M}_\odot\,{\rm yr}^{-1}$, in good agreement with the previous estimate.

5.2 Comparison with other IR galaxy populations

SST J1604+4304 is a dusty, super metal-rich, young galaxy at $z = 1.135$ with $E_{B-V} = 0.8$, metallicity 2.5 $\,{\rm Z}_\odot$ and an age 40–200 Myr. The age is comparable to young, optical selected populations like Lyman-α emitters (LAEs) and Lyman break galaxies (LBGs). Studying the $z \sim 3$ LAE sample, Gawiser et al. (2006) inferred ages of the order of 100 Myr with stellar masses $5 \times 10^8\,{\rm M}_\odot$ and no dust extinction. Pirzkal et al. (2007) showed that $4 < z < 5.7$ LAEs had very young ages a few Mys with stellar masses 10^6–$10^8\,{\rm M}_\odot$. Sawicki & Yee (1998), studying $z > 2$ LBGs, found that their LBGs were dominated by young stellar populations with ages <200 Myr with stellar masses several $\times 10^9\,{\rm M}_\odot$ and moderate dust extinction typically $E(B-V) \sim 0.3$. The $z = 2$–3.5 sample of LBGs by Papovich, Dickinson & Ferguson (2001) has ages of 30 Myr to 1 Gyr with stellar masses 10^9–$10^{11}\,{\rm M}_\odot$ with $E(B-V) = 0.0$–0.4. SST J1604+4304, having a stellar mass 6–13 $\times\, 10^{10}\,{\rm M}_\odot$, is more massive and more dusty than these optically selected galaxies.

SST J1604+4304 having $f_\nu(24\,\mu{\rm m})/f_\nu(R) > 1000$ meets the criteria for 24 μm selected high-redshift ($z \sim 2$) DOGs. DOGs and SMGs have extremely large $L_{\rm ir}/L_{\rm B}$ which cannot be accounted for by redshifting local ULIRGs (Dey et al. 2008; Pope et al. 2008b). Dey et al. (2008) found nearly all of DOGs are ULIRGs with $L_{\rm ir} > 10^{12}\,{\rm L}_\odot$ and more than half of these have $L_{\rm ir} > 10^{13}\,{\rm L}_\odot$. The IR luminosity of radio-identified SMGs ranges $L_{\rm ir} = 2 \times 10^{11}$–$10^{14}\,{\rm L}_\odot$ (Chapman et al. 2005). A SFR 1000 $\,{\rm M}_\odot\,{\rm yr}^{-1}$, which corresponds to $L_{\rm ir} = 5 \times 10^{12}\,{\rm L}_\odot$ (Kennicutt 1998), builds up a stellar mass of $10^{11}\,{\rm M}_\odot$ in 100 Myr. Thus, it is considered that DOGs and SMGs are progenitors of present-day massive galaxies. If ages of stellar populations in DOGs and SMGs are derived, as we did for SST J1604+4304 by measuring the stellar absorption lines, the evolutionary link of DOGs and SMGs to normal ULIRGs and optically selected galaxies will be better understood.

5.3 SNe for dust and metal production

In SST J1604+4304 with an age 40–200 Myr, most of the dust would be formed by Type II supernovae (SNe II), because low-mass stars had not evolved to form dust in the expanding envelope. This may be the reason why our best model results in poor goodness of fit $\chi^2_\nu({\rm min}) = 5.2$. The Calzetti's extinction law may not be applicable to such young galaxies, because dust grains in local starbursts would be dominated by those formed in the outflows of low-mass stars and not by SNe II dust. In this regard, it is of great interest to use the SED of SST J1604+4304 to test extinction laws such as those calculated by Hirashita et al. (2005, 2008) that are predicted for dust formed in SNe II ejecta (Nozawa et al. 2003).

Our best model is the instantaneous-burst model with an age 40 Myr with a stellar mass $6.4 \pm 2.3 \times 10^{10}\,{\rm M}_\odot$ at $t = 0$. The metallicity is 2.5 $\,{\rm Z}_\odot$ and the dust mass is $M_{\rm dust} = 2.0 \pm 1.0 \times 10^8\,{\rm M}_\odot$. Until 40 Myr after the onset of the starburst, stars with a mass $>8\,{\rm M}_\odot$ died with a SN explosion. The number of stars evolved into SNe in 40 Myr is 7.6×10^8 or 19 SNe per year. Adopting the nucleosynthesis models by Nomoto et al. (2006), the total yield is 0.09–0.11 and the metal yield is 0.016–0.020 for the Chabrier IMF.[5] The gas and stellar metallicities can be estimated applying simply analytical models based on the instantaneous recycling approximation. The gas metallicity is expressed as $Z_{\rm g}(t) = y(t)\,\ln\,[1/f(t)]$ where $f(t)$ is the ratio of the gas mass to the galaxy mass, and $y(t)$ is the ratio of the rate at which the metal is produced by the events of nucleosysnthesis and ejected into the interstellar gas to the rate at which hydrogen is removed from the interstellar gas by star formation (Searle & Sargent 1972). The stellar metallicity Z_* is derived from $S(Z)/S_1 = (1 - f_1^{Z/Z_1})/(1 - f_1)$ and $Z_* = \int_0^{Z_1} Z dS(Z) / \int_0^{Z_1} dS(Z)$, where $S(Z)$ is the total mass of stars born up to a time when the metal abundance reached to the value Z, and S_1, Z_1, f_1 denote $S(t_1)$, $Z(t_1)$, $f(t_1)$, respectively (Pagel & Patchett 1975). In our case, t_1 is a time when the stellar metallicity reached to $Z_* = 2.5\,{\rm Z}_\odot$. When the gas mass is reduced to $f = 0.3$, we have $Z_* = 2.4$–$2.7\,{\rm Z}_\odot$ and $Z_{\rm g} = 4.5$–$5.1\,{\rm Z}_\odot$. The inferred galaxy mass is 1.2 times the stellar mass at $t = 0$, because the total mass ejected from stars at the events of SN explosions into

[5] The original yields are given for the Salpeter IMF. These are converted to the Chabrier IMF by simply multiplying 1.64 to adjust the difference in the mass fraction of stars from 8–100 $\,{\rm M}_\odot$ to those from 0.1–100 $\,{\rm M}_\odot$.

the interstellar gas is 0.1 per unit stellar mass at $t = 0$. The total gas mass is $2.3 \times 10^{10}\,M_\odot$. The gas-to-dust mass ratio is then 120 ± 73, which is comparable to the value obtained in a $z = 1.3$ HyLIRG (198 ± 53) by Iono at al. (2006).

The dust production rate is $0.24 \pm 0.12\,M_\odot$ per SN. This is consistent with the numerical results of dust formation in SNe; for progenitor masses ranging 13–30 $M_\odot$, 2–5 per cent of the progenitor mass is locked into dust grains at SN explosions (Nozawa et al. 2003), 20–100 per cent of which is destroyed by processing through the collisions with the reverse shocks resulting from the interaction of SN ejecta and with the ambient medium (Nozawa et al. 2007).

5.4 Foreground dust screen

As demonstrated in Section 3.2, a foreground dust screen geometry is plausible for SST J1604+4304. This indicates that dust is depleted in the starburst site and the stellar spectra are reddened by the foreground dust screen which enclosed the starburst site. Let's suppose a spherical shell with a radius l for the dust distribution, then we observe $f_\nu = 4\tau_\nu B_\nu(T_{\rm dust})\pi(l/D)^2$ in the rest frame, where the thickness of the shell is τ_ν which is 0.0074 at rest 80 μm corresponding to $E(B-V) = 0.83$ with $R_V = 4.05$ (Draine 2003), D is the distance from the observer to SST J1604+4304 and $T_{\rm dust} = 32.5$–35 K. Converting this relation into the observer's frame, we obtain the radius $l = 4.5$–5.5 kpc or 0.56–0.65 arcsec. This is comparable to the optical size of SST J1604+4304 which is approximately 1.2×0.5 arcsec^2 in the I_{814} band. This supports the view that the galaxy is surrounded by the shell. Further support is the fact that there are no significant colour gradients across the galaxy in the *HST* images.

5.5 Evolutionary link to other galaxy populations

As discussed by Calzetti (2001), starburst environments are rather inhospitable to dust; dust grains in the starburst site can be transported to a large distance in a relatively short time by radiation pressure (Ferrara et al. 1991; Venkatesan, Nath & Shull 2006), as well dust grains that formed at SN explosions are processed and evolve in SN remnants (Nozawa et al. 2007) – small size grains are quickly destroyed in SN remnants by sputtering. Thus, a cavity-shell structure is a natural geometry for the dust distribution in star-forming galaxies; the starburst site is inside the cavity where dust is depleted, and the opaque dust shell is surrounding the cavity. The shell is observed as a foreground screen. Such foreground screens were found in local starburst galaxies (Calzetti et al. 1994; Meurer et al. 1995). In the foreground screen of SST J1604+4304, the dust would be unevenly distributed; we are only looking at part of the starburst site at UV and optical wavelengths through relatively transparent holes with $E(B-V) = 0.8$, and the other part is completely obscured at these wavelengths. This explains that $L_{\rm ir}$ is two times greater than the stellar luminosity derived from the broad-band SED analysis.

Venkatesan et al. (2006) and Nozawa et al. (2007) suggest that dust created in the first SN explosions can be driven through the interior of the SN remnants and accumulated in the SN shells, where second-generation stars may form in compressed cooling gases. Hence, galaxies may be observed as dust-free objects at the very beginning. When much dust formed in SN ejecta, the starburst site would become completely obscured by dust at UV to near-IR wavelengths. This stage would correspond to extremely dusty objects like DOGs and SMGs. Then, the galactic winds would turned on. Heckman et al. (1990) discussed that the galactic winds or superwinds frequently observed in starbursts and ULIRGs will sweep out any diffuse interstellar matter from the starburst site. Such galactic winds will be turned on when the thermal energy of the gas heated by SN explosions exceeds the gravitationally binding energy of the gas. According to the models for chemical evolution of elliptical galaxies by Arimoto & Yoshii (1987), galactic winds turn on later in more massive galaxies. The onset of a galactic wind is 350 Myr for a $10^{11}\,M_\odot$ galaxy, and the metallicity increases up to more than the solar value. These predictions seem to agree well with the age and the metallicity observed in SST J1604+4304, in which the galactic wind would just turn on and dust grains in the opaque shell are pushed and moved outwards, creating partially transparent holes in the shell. This picture is consistent with the fact that dusty objects are deemed to be more abundant in massive galaxies than in less massive galaxies, although mid- and far-IR observations are strongly biased to IR-luminous objects. This observational trend is expected, because galactic winds turn on later and thus the dust shell becomes more opaque for more massive galaxies, resulting in longer time of the dust-obscured stage. This may be the reason why DOGs and SMGs are so IR-luminous and massive.

5.6 Impact by an obscured AGN

What would happen if the missing 1/2 of the bolometric luminosity comes from an AGN? In this case, the stellar mass ranging 0.1–$8\,M_\odot$ is reduced to one half of that for the pure star formation. The number of SNe is also reduced by the same amount, while the dust mass does not change. Thus, the dust production rate is increased by a factor of 2, i.e. $0.48 \pm 0.24\,M_\odot$ per SN. This is within a range consistent with the model predictions (Nozawa et al. 2003; Nozawa et al. 2007). The metallicity is the same as derived for pure star formation, because the SN ejecta mass is also reduced by a factor of 2. If the AGN shines at the Eddington rate, the mass of the AGN is $2.5 \times 10^7\,M_\odot$.

ACKNOWLEDGMENTS

We are grateful to Y. Tsuzuki for assisting the *UKIRT* observation and to the anonymous referee for very useful comments. This work has been supported in part by Grants-in-Aid for Scientific research (17104002, 20340038) and Specially Promoted Research (20001003) from JPSP.

REFERENCES

Arimoto N., Yoshii Y., 1987. A&A, 173, 23
Armus L., Neugebauer G., Soifer B. T., Matthews K., 1995, AJ, 110, 2610
Avni Y., 1976, ApJ, 210, 642
Borys C. et al., 2006, ApJ, 636, 134
Bruzual G., 1983, ApJ, 273, 105
Bruzual G., Charlot S., 2003, MNRAS, 344, 1000
Calzetti D., 2001, PASP, 113, 1449
Calzetti D., Kinney A. L., Storchi-Bergmann T., 1994, ApJ, 429, 582
Carico D. P., Sanders D. B., Soifer B. T., Matthews K., Neugebauer G., 1990, AJ, 100, 70
Chabrier G., 2003, PASP, 115, 763
Chapman S. C., Blain A. W., Smail I., Ivison R. J., 2005, ApJ, 622, 772
Chary R., Elbaz D., 2001, ApJ, 556, 562
Dale D. A. et al., 2007, ApJ, 655, 863
Desai V. et al., 2006, ApJ., 641, 133
Dey A. et al., 2008, ApJ, 677, 943
Draine B. T., 2003, ARA&A, 41, 241
Elbaz D. et al., 1999, A&A, 351, L37

Fazio G. G. et al., 2004, ApJS, 154, 10
Ferrara A., Ferrini F., Barsella B., Franco J., 1991, ApJ, 381, 137
Gal R. R., Lubin L. M., 2004, ApJ, 607, L1
Gawiser E. et al., 2006, ApJ, 642, L13
Genzel R., Cesarsky C. J., 2000, ARA&A, 38, 761
Heckman T. M., Armus L., Miley G. K., 1990, ApJS, 74, 833
Héraudeau P. et al., 2004, MNRAS, 354, 924
Hirashita H., Nozawa T., Kozasa T., Ishii T. T., Takeuchi T. T., 2005, MNRAS, 357, 1077
Hirashita H., Nozawa T., Takeuchi T. T., Kozasa T., 2008, MNRAS, 384, 1725
Hughes D. H., Gear W. K., Robson E. I., 1994, MNRAS, 270, 641
Iono D. et al., 2006, PASJ, 58, 957
Ivison R. J. et al., 2004, ApJS, 154, 124
Kawara K. et al., 1998, A&A, 336, L9
Kawara K. et al., 2004, A&A, 413, 843
Kennicutt R. C., 1998, ARA&A, 36, 189
Klaas U., Haas M., Heinrichsen I., Schulz B., 1997, A&A, 325, L21
Kobayashi Y. et al., 1998, Proc. SPIE, 3352, 120
Leeuw L. L., Robson E. I., 2009, AJ, 137, 517
Lubin L. M., Mulchaey J. S., Postman M., 2004, ApJ, 601, L9
Majewski S. R., Kron R. G., Koo D. C., Bershady M. A., 1994, PASP, 106, 1258
Margoniner V. E., Lubin L. M., Wittman D. M., Squires G. K., 2005, AJ, 129, 20
Matsuoka Y. et al., 2008, ApJ, 685, 767
Meurer G. R., Heckman T. M., Leitherer C., Kinny A., Robert C., Garnett D. R., 1995, AJ, 110, 2665
Minezaki T., Yoshii Y., Kobayashi Y., Enya K., Suganuma M., Tomita H., Aoki T., Peterson B. A., 2004, ApJ, 600, L35
Nomoto K., Tominaga N., Umeda H., Kobayashi C., Maeda K., 2006, Nucl. Phys. A, 777, 424
Nozawa T., Kozasa T., Umeda H., Maeda K., Nomoto K., 2003, ApJ, 598, 785
Nozawa T., Kozasa T., Habe A., Dwek E., Umeda H., Tominaga N., Maeda K., Nomoto K., 2007, ApJ, 666, 955
Oliver S. J. et al., 1997, MNRAS, 289, 471
Oyabu S. et al., 2005, AJ, 130, 2019
Oyabu S., Kawara K., Tsuzuki Y., Matsuoka Y., Sameshima H., Asami N., Ohyama Y., 2009, ApJ, 697, 452
Pagel B. E. J., Patchett B. E., 1975, MNRAS, 172, 13
Papovich C., Dickinson M., Ferguson H. C., 2001, ApJ, 559, 620
Park S. Q. et al., 2008, ApJ, 678, 744
Pirzkal N., Malhotra S., Rhoads J. E., Xu C., 2007, ApJ, 667, 49
Polletta M., Weedman D., Hönig S., Lonsdale C. J., Smith H. E., Houck J., 2008, ApJ, 675, 960
Pope A. et al., 2008a, ApJ, 675, 1171
Pope A. et al., 2008b, ApJ, 689, 127
Puget J. L. et al., 1999, A&A, 345, 29
Rabin D., 1982, ApJ, 261, 85
Reddy N. A., Steidel C. C., Fadda D., Yan L., Pettini M., Shapley A. E., Erb O. K., Adelberger K. L., 2006, ApJ, 644, 792
Rigopoulou D., Lawrence A., Rowan-Robinson M., 1996, MNRAS, 278, 1049
Sanders D. B., Mirabel I. F., 1996, ARA&A, 34, 749.
Santos J. F. C., Piatti A. E., 2004, A&A, 428, 79
Sato Y., et al., 2003, A&A, 405, 833
Sawicki M., Yee H. K., 1998, AJ, 115, 1339
Schneider P., Ehlers J., Falco E. E., 1992, Gravitational Lenses. Springer-Verlag, Berlin
Searle L., Sargent W. L. W., 1972, ApJ, 173, 25
Serjeant S. et al., 2000, MNRAS, 316, 768
Stern D. et al., 2005, ApJ, 631, 163
Soifer B. T., Boehmer L., Neugebauer G., Sanders D. B., 1989, AJ, 98, 766
Soifer B. T., Helou G., Werner M., 2008, ARA&A, 46, 201
Taniguchi Y. et al., 1997 A&A, 328, L9
Telfer R. C., Zheng W., Kriss G. A., Davidsen A. F., 2002, ApJ, 565, 773
Venkatesan A., Nath B. B., Shull J. M., 2006, ApJ, 640., 31
Weedman D., Charmandaris V., Zezas A., 2004, ApJ, 600, 106
Werner M. W. et al., 2004, ApJS, 154, 1
White R. L., Becker R. H., Helfand D. J., Gregg M. D., 1997, ApJ, 475, 479
Willner S. P., Soifer B. T., Russell R. W., Joyce R. R., Gillett F. C., 1977, ApJ, 217, L121
Yagi M., Kashikawa N., Sekiguchi M., Doi M., Yasuda N., Shimasaku K., Okamura S., 2002, AJ, 123, 66
Yan L. et al., 2007, ApJ, 658, 778
Yoshii Y., 2002, in Sato K., Shiromizu T., eds, New Trends in Theoretical and Observational Cosmology. Universal Press, Tokyo, p. 235

This paper has been typeset from a TEX/LATEX file prepared by the author.